Stability of Planar Parallel Flows

In this section we examine some of the results obtained from the linear stability analyses described in section (Bkc). It is convenient to begin with the data for boundary layers presented in Figures 1 to 4. The equations governing the perturbations in section (Bkc) suggest that it is convenient and appropriate to non-dimensionalize the coordinate x by using a surrogate parameter in the form of the displacement thickness, δ_D, and to non-dimensionalize this in the form of $\delta_D U/\nu$ which is a Reynolds number based on the displacement thickness and the velocity, U, at the edge of the boundary layer. Thus $\delta_D U/\nu$ will represent the distance, x, in the data that follows. Moreover, a convenient non-dimensional frequency is $\omega_R \nu/U^2$.
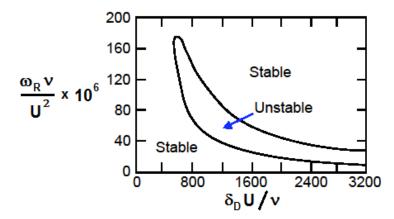

Figure 1: Neutral stability boundary ($k_I = 0$) for the Blasius boundary layer velocity profile in a graph of the perturbation frequency, $\omega_R \nu/U^2$, plotted against the surrogate distance parameter, $\delta_D U/\nu$.

As a first example of the results of a stability calculation, Figure 1 presents the neutral stability contour ($k_I = 0$) for the Blasius boundary layer velocity profile in a graph of the potential perturbation frequency, $\omega_R \nu/U^2$, plotted against the surrogate distance parameter, $\delta_D U/\nu$. The regions of stable behavior surround a region of instability and the neutral stability line demonstrates that the boundary layer, which is stable when δ_D is small, first becomes unstable when $\delta_D U/\nu \approx 600$ as we can see by constructing a vertical tangent to the neutral stability curve. Since we have seen in section (Bjd) that $\delta_D = 1.72(\nu x/U)^{\frac{1}{2}}$ for the Blasius boundary layer it follows that this will first become unstable when the distance x from the leading edge increases to a value given by

$$\left(\frac{Ux}{\nu}\right) = (Re_x) = \left(\frac{600}{1.72}\right)^2 = 1.22 \times 10^5 \tag{Bkd1}$$

where Re_x denotes the Reynolds number based on U and x. It also follows that the first frequency which becomes unstable is given by the point where the vertical tangent touches the neutral stability curve and from Figure 1 that frequency is given by

$$\omega_R \approx 1.6 \times 10^{-4}\frac{U^2}{\nu} \tag{Bkd2}$$

Since it is that frequency which is first amplified, it is usually that frequency that is observed experimentally during the first stages of transition. This assumes that the inherent noise available for amplification is at least broadband if not white.
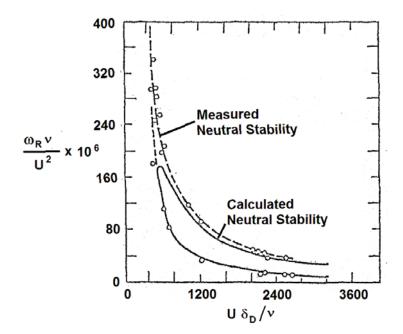
Figure 2: As Figure 1, comparing the calculated neutral stability boundary with experimental measurements. Adapted from Schlichting (1960).
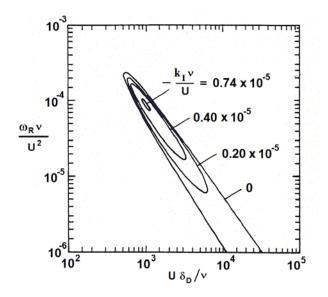

Figure 3: Spatial amplification for the Blasius boundary layer velocity profile in a graph of the perturbation frequency, $\omega_R \nu/U^2$, plotted against the surrogate distance parameter, $\delta_D U/\nu$, showing contours of several amplification rates, $-k_I \nu/U$, as indicated. Adapted from Jaffe *et al.* (1970); see also Sherman (1990).

Figure 2 shows a comparison between the analytical neutral stability curve presented in Figure 1 and some experimental observations of that neutral stability boundary. The agreement is good and any discrepancy can probably be attributed to the difficulty of determining exactly where the instability begins.

To proceed beyond the neutral stability curve and calculate the growth of the noise downstream of the onset of amplification as we discuss in the next section (Bke), knowledge of the amplification rates inside the neutral stability curve are needed. For the Blasius boundary layer profile, some contours of non-zero non-dimensional amplification rates, $-k_I \nu/U$, are shown in Figure 3. How this data can be used is discussed in the section that follows.
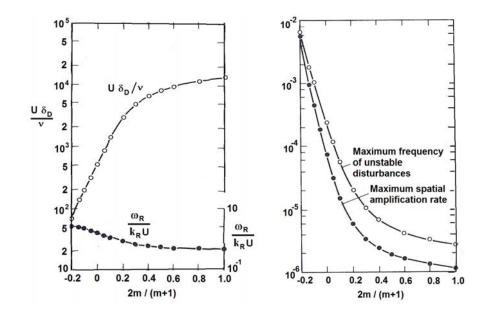
Figure 4: Spatial amplification data for the Falkner-Skan boundary layer velocity profiles. Left: values of the critical Reynolds numbers, $U\delta_D/\nu$ (left scale), and the corresponding disturbance velocity, ω_R/Uk_R (right scale), plotted against $2m/(m+1)$. Right: values of the maximum frequency of unstable perturbations, $\omega_R\nu/U^2$, and the maximum spatial amplification rates, $-k_I\nu/U$, as functions of $2m/(m+1)$. Adapted from Sherman (1990).

Turning to other velocity profiles for boundary layers, Figure 4 presents some data for various Falkner-Skan profiles characterized by the parameter m or, more specifically, by $2m/(m+1)$ which is related to the half-angle of the wedge on which such a profile would occur, $\beta\pi/2$, by $\beta = 2m/(m+1)$. The left graph presents values of the critical Reynolds numbers, $U\delta_D/\nu$ (left scale), and the corresponding disturbance velocity, ω_R/Uk_R (right scale). The right graph presents values of the maximum frequency of unstable perturbations, $\omega_R\nu/U^2$, and the maximum spatial amplification rates, $-k_I\nu/U$. Note that the larger the acceleration of the external velocity, U, the more stable the flow becomes with larger critical Reynolds numbers, $\delta_D U/\nu$, and smaller maximum amplification rates, $-k_I\nu/U$. Conversely, when the external flow is decelerating (m becomes negative), the boundary layer becomes much less stable and the amplification rates become much larger. We comment in the next section on how this Falkner-Skan data has been used in efforts to predict the progress of transition to turbulence.

As another example, we turn to the stability of an interfacial boundary layer profile with zero shear stress at $y = 0$. This anticipates the development of Tollmein-Schlichting waves on the gas/liquid free surface in a liquid boundary layer flow that separates after developing on the surface of an object in a uniform stream. These can be seen in Figures 5 and 6 which are photographs of the surface of cavities behind an ogive and a sphere showing the waves appearing just after the free surface leaves the object surface (Brennen 1970). The same kind of instability waves can be observed on the surface of a liquid jet provided the boundary layer prior to separation is laminar; Figure 7 exhibits such waves (Hoyt and Taylor 1977).

A general stability eigenvalue diagram for the spatial or temporal stability of an interfacial free surface boundary layer is shown in Figure 10; it is a graph of the imaginary wavespeed, $c_I/\Delta U$, plotted against $(U - c_R)/\Delta U$ ($\omega = kc$) in which contours of real and imaginary wavenumbers, bk_R and bk_I have been plotted. The fluid velocity far from the interface is U, ΔU is the velocity at the interface and b is the half-width of the velocity profile.

Finally, we present in Figure 10, the stability graph for a planar Poiseuille flow between two plates a distance $2h$ apart (Figure 9). The line for various amplification rates, $-\omega_I U/k_R h$, are plotted in a graph of the dimensionless perturbation wavenumber, $k_R h$, against the Reynolds number, Uh/ν, where U is the
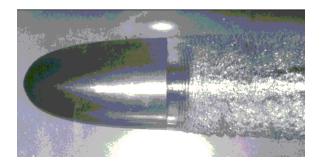
Figure 5: Flow of water past an ogival headform showing the growing Tollmein-Schlichting waves on the interfacial layer just after separation (Brennen 1970).

Figure 6: Flow of water past a spherical headform showing the growing Tollmein-Schlichting waves on the interfacial layer just after separation (Brennen 1970).

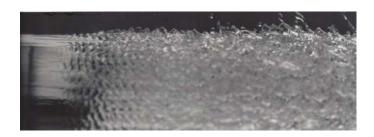maximum or centerline velocity of the flow.

Figure 7: Water jet emerging from a laminar nozzle (Hoyt and Taylor 1977).
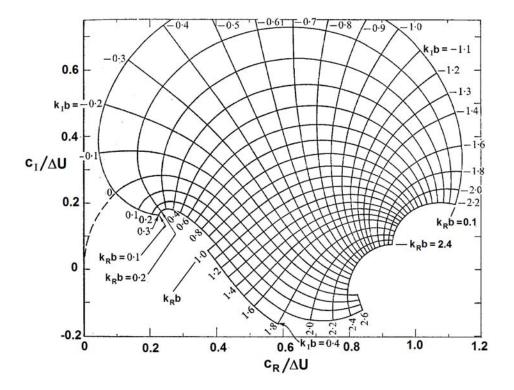
Figure 8: General amplification chart for the spatial or temporal stability of an interfacial boundary layer with a free surface in a graph of the imaginary wavespeed, $c_I/\Delta U$, plotted against $(U - c_R)/\Delta U$. Contours of real and imaginery wavenumbers, bk_R and bk_I are shown. Adapted from Brennen (1970).
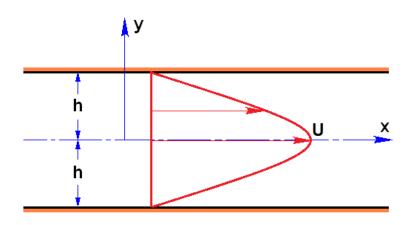

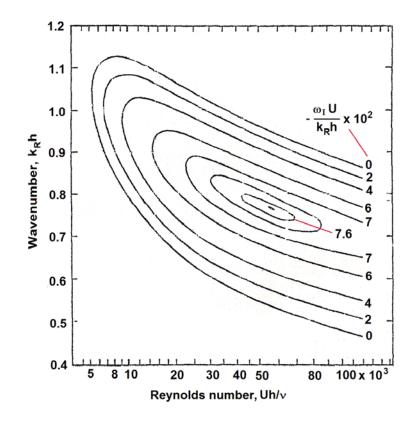Figure 9: Planar Poiseuille flow between two flat plates.

Figure 10: Spatial amplification for planar Poiseuille flow in a graph of the perturbation wavenumber, $k_R h$, plotted against the Reynolds number, Uh/ν. Contours of several amplification rates, $-\omega_I U/k_R h$, are shown. Adapted from Shen (1954).